

Anthony J. Chirico III

Mem. ASME
Aircraft Group,
MOOG, Inc.,
East Aurora, NY 14052

e-mail: tchirico2@moog.com

Jason R. Kolodziej¹

Assistant Professor
Mem. ASME

Department of Mechanical Engineering,
Rochester Institute of Technology,
Rochester, NY 14623
e-mail: jrkeme@rit.edu

A Data-Driven Methodology for Fault Detection in Electromechanical Actuators

This research investigates a novel data-driven approach to condition monitoring of electromechanical actuators (EMAs) consisting of feature extraction and fault classification. The approach is able to accommodate time-varying loads and speeds since EMAs typically operate under nonsteady conditions. The feature extraction process exposes fault frequencies in signal data that are synchronous with motor position through a series of signal processing techniques. A resulting reduced dimension feature is then used to determine the condition with a trained Bayesian classifier. The approach is based on signal analysis in the frequency domain of inherent EMA signals and accelerometers. For this work, two common failure modes, bearing and ball screw faults, are seeded on a MOOG MaxForce EMA. The EMA is then loaded using active and passive load cells with measurements collected via a dSPACE data acquisition and control system. Typical position commands and loads are utilized to simulate “real-world” inputs and disturbances and laboratory results show that actuator condition can be determined over a range of inputs. Although the process is developed for EMAs, it can be used generically on other rotating machine applications as a Health and Usage Management System (HUMS) tool. [DOI: 10.1115/1.4026835]

1 Introduction

Electromechanical actuators are the next progression in flight control actuators as the industry continues to move toward the goal of all electric aircraft [1]. Currently, these types of actuators are used mainly on secondary flight control surfaces, such as spoilers and horizontal tail stabilizers, but not on primary surfaces. This is mainly due to the failure modes of the EMAs that cannot be mitigated in flight as easily as its hydraulic actuator counterparts. Specifically, the risk of jamming can cause a flight control surface to lock in place and compromise the safe operation of the flight control system. However, there are many benefits for more electric aircraft such as overall weight reduction, increased reliability, better maintainability, reduced operating costs, and increased safety [2].

Integrated health management (IHM) offers an advantage to make the adaptation of EMAs in critical applications more practical by indicating the need for service prior to catastrophic EMA failure and disruption of service. IHM is also a viable progression from statistical (or schedule)-based maintenance to condition-based maintenance (CBM) for flight control actuation systems. In CBM, the condition of the equipment is monitored and maintenance is based on the assessed condition. As such, IHM systems must be capable of monitoring degradation and detecting faults at the early stages of its development, in advance of full functional failure.

1.1 Recent Advancements in EMA Health Monitoring. IHM is usually comprised of data acquisition, signal reduction/feature extraction, condition assessment, fault diagnosis, prognostics, and decision support [3]. The most common approaches for EMA IHM to date have been model based and data driven. Model-based approaches typically involve the creation of an accurate mathematical model to predict the outputs to a set of inputs

for assessing health. For instance, the error between the actual outputs and the model predicted outputs can be used to estimate system parameters such as damping and efficiency. The estimated parameters can then be compared to the parameters of a healthy system to determine if there is a fault [4,5].

Noted benefit to the model-based approach was that failure modes are traced back to model parameters to lend insight into the failure for fault diagnosis. In addition, the severity of the fault could be characterized by the deviation of the estimated parameters to the healthy EMA parameters that were previously characterized. This type of approach is also suited to predict health over multiple nonsteady operating conditions, but only as long as command and disturbances can be measured or calculated. The drawback of the model-based approach is that models are often complex and must be validated. As such, the models are then very specific to the application and new models must be created and validated for each new application. In addition, implementing this type of scheme in an EMA controller, for instance, would require a significant amount of processing capability when added to the normal control and management schemes typically employed for flight control actuators.

As opposed to model-based techniques, data-driven approaches operate directly on signal data, using signal processing techniques and “black box” models to expose patterns/signatures in signal data that give insight into machine condition. Data-driven approaches are an attractive option to IHM since it does not require complex models and can be applied to many types of systems.

Within the field of actuator fault detection and isolation, data-driven techniques have included wavelet analysis, statistical analysis, neural network analysis, and frequency domain analysis. For instance, Balaban et al. [6] use several statistical features including accelerometer sensor standard deviation, thermocouple temperature deviation from nominal, and thermocouple drift. In Ref. [7], vibration sensors are used to monitor fault frequencies that would appear as components started to wear. In Ref. [8], the degree of overlap of signal probability densities between a baseline “healthy” EMA set and EMAs with artificially aged capacitors during steady state operating conditions was used to assess condition.

¹Corresponding author.

Contributed by the Dynamic Systems Division of ASME for publication in the JOURNAL OF DYNAMIC SYSTEMS, MEASUREMENT, AND CONTROL. Manuscript received April 30, 2013; final manuscript received February 6, 2014; published online April 28, 2014. Assoc. Editor: Qingze Zou.

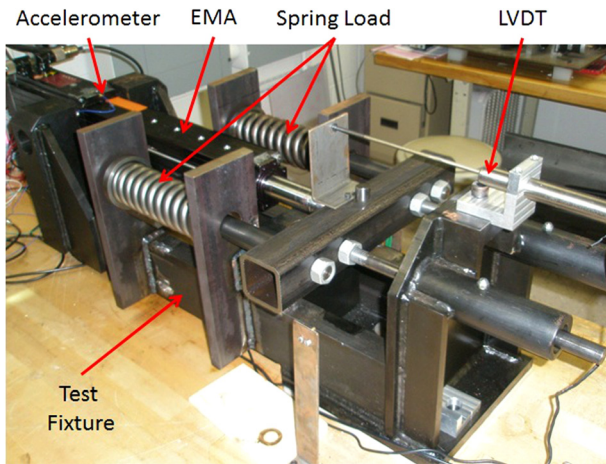


Fig. 1 MOOG MaxForce EMA in test fixture

These works focused primarily on feature extraction, but several other works also included health classification and prognostics, such as Ref. [9], which use FFT-based feature techniques in addition to a neural network error tracking method. Automated health classification was accomplished by a fuzzy logic classifier with data fusion along with a prognostics model using a Kalman filter feature-based state space tracking routine. Another approach taken by Brown et al. [10] used the Hilbert transformation for identifying turn-to-turn winding faults for a brushless dc motor in an EMA and a particle filter for anomaly detection and prognostics.

One of the main problems cited in data-driven approaches is the masking of defects due to differing and nonconstant operating conditions. For instance, as motor speed and load vary, the amount of vibration changes and fault frequencies are spread throughout the frequency spectrum, making fault identification difficult. This problem was also cited by Romeral et al. [11] who propose the use of the discrete wavelet transform to show how frequency content varies with time for nonstationary conditions. Another approach to deal with nonsteady motor velocities is proposed by Huh et al [12] who use a digital resampling method to map signals from the time domain to the spatial domain since many faults in rotating machinery are synchronous with motor position.

Another issue that arises in EMA health monitoring is the permissibility of using specialized sensors, so emphasis has been placed on the ability to use only available EMA signals. A technique known as motor current signature analysis has been shown to be successful for identifying faults in components that are part of motor control systems, such as motor, bearing and gear faults [13]. Another challenge is due to the potentially large number of feature variables that result from using multiple feature extraction methods. Principal components analysis (PCA) is a way of identifying patterns in data and reducing the dimensionality of the data. Another important aspect of PCA is that it transforms a set of possibly correlated variables into a set of principal components that are linearly uncorrelated. The technique has been used for various applications, including face recognition and image compression,

but also in fault detection and classification. For instance, Malhi and Gao [14] use PCA as a feature selection scheme for contending features in bearing defect classification.

1.2 Objectives and Outline. This research focuses on the feature extraction and fault diagnosis portions of the IHM process for condition monitoring of electromechanical actuators. The goal is to improve upon previous research in EMA health monitoring by creating a data-driven approach that is able to handle non-steady motor speeds and multiple loading conditions, is able to use standard and nonstandard EMA sensors, and can handle multiple contending features.

This paper is organized as follows: The need for EMA health management has been presented with a comprehensive review of current health monitoring research including the challenges that exist. In the remainder of the paper, the proposed approach to feature extraction and fault classification is presented and then demonstrated via simulation using generated data. This is followed by experimental testing of the approach on MOOG Max-Force EMAs that result from the use of two laboratory test cells, passive (Fig. 1) and active (Fig. 12). Lab generated EMA data are obtained over various operating conditions using a healthy EMA, one seeded with a bearing fault and one seeded with a ball screw fault. The performance of the approach is demonstrated by the percentage of false positives and false negatives. Finally, plans for improvement and future work are given.

2 The Proposed EMA Fault Detection Approach

The fault detection scheme after data acquisition is comprised of feature extraction and fault classification as shown in Fig. 2. The objective is to assign a class that relates to the condition of the EMA based on the sensor measurement \mathbf{x} . Ideally, the predicted condition matches the true condition of the EMA. The system from which measurements are obtained include the EMA to be monitored and the associated environment (controller, load, etc.). The system is excited with inputs \mathbf{r} and results in the measurement output, \mathbf{x} . The measurement data are transformed after data acquisition by the feature extraction process in order to give insight into the condition of the EMA. It also serves to reduce the size of the data prior to classification. A feature vector, \mathbf{z} , is then input to a classifier which uses these data to predict the condition of the EMA $w(\mathbf{z})$ from a possible set of conditions $w \in \{w_1, w_2, w_3, \dots\}$.

2.1 Feature Extraction. In feature extraction, the measurement data are transformed in order to expose patterns and signatures within the data that give insight into the condition of the EMA. The feature extraction method proposed in this paper is aimed at exposing faults that produce fault signatures in the frequency domain that are synchronous with motor position. Frequency analysis of vibration and motor current signals has been shown to be effective in exposing fault signatures in rotating machine equipment to isolate various faults and failures at the incipient stage, including: bearing and gear faults, screw defects, stator and armature faults, broken rotor bar and end ring faults, and eccentricity faults, among others [15–18].

For instance, the mechanical defect frequency produced by an inner race defect on a ball bearing is given by



Fig. 2 EMA fault detection architecture

$$f_{\text{IR}} = \frac{n}{2} f_r \left(1 - \frac{\text{BD}}{\text{PD}} \cos \phi \right) \quad (1)$$

where n equals the number of rotating elements (balls), BD is the ball diameter, PD is the pitch diameter, ϕ is the contact angle, and f_r is the motor speed expressed in Hz. The defect appears in the motor current signal at the following frequency:

$$f_c = |f_e \pm m f_{\text{IR}}| \quad (2)$$

where m is an integer accounting for the harmonic contributions, and f_e is the fundamental current frequency. For a three phase permanent magnet synchronous motor (PMSM), the fundamental current frequency is related to the rotor frequency by

$$f_e = \frac{p}{2} f_r \quad (3)$$

where p is the number of motor poles. Therefore, Eq. (2) becomes

$$f_c = f_r \left| \frac{p}{2} \pm \frac{m f_{\text{IR}}}{f_r} \right| \quad (4)$$

In summary, this research focuses on the feature extraction architecture shown in Fig. 3. Signal data that are originally sampled according to a fixed sampling time interval are resampled to the position domain. The signal is then transformed to the frequency domain by computing the power spectral density (PSD). A binning process groups the frequency content of the filtered PSD signal into energy bins and then the data are reduced by a feature space transformation process. The transformation matrix is optimized using training samples so that the most important information in the data is retained—much like in image compression.

2.1.1 Resampling Technique. Due to the operation of the motor, many electrical and mechanical fault signatures in rotating equipment are synchronized with the angular motor position. Since normal operation of an EMA for many applications involves varying motor velocities, fault signatures will be periodic with motor position, but not in time. If signals are acquired according to the sampling period T_s , a post processing method must exist to resample the signal according to the spatial sampling period θ_s to expose the periodic nature of the fault. Various interpolation and filtering techniques may be used, for instance, the following equation:

$$x(n) = x(k) + \frac{x(k) - x(k-1)}{\theta_c(k) - \theta_c(k-1)} (n\theta_s - \theta_c(k-1)) \quad (5)$$

where θ_c is the time sampled cumulative motor angle. The equation maps the time sampled signal $x(k) = x(kT_s)$ to the spatially sampled signal $x(n) = x(n\theta_s)$.

2.1.2 PSD. The resampled signal can be processed by many frequency analysis methods. In this work, a PSD technique is applied. The two-sided power spectrum of a discrete signal is

$$S_{xx}(k) = \frac{2}{w_f L} X_w(k) X_w^*(k) \quad -L/2 < k \leq L/2 \quad (6)$$

where L is the number of samples and $X_w(k)$ is the discrete Fourier transform of the windowed signal $x_w(n)$

$$x_w(n) = w(n)x(n) \quad (7)$$

For instance, a rectangular window results when $w(n) = 1$, or a Hanning window of length L may be used to reduce the effect of leakage in out of band frequencies as in the following equation:

$$w(n) = \frac{1}{2} \left(1 - \cos \left(2\pi \frac{n}{L} \right) \right) \quad (8)$$

The window factor w_f in Eq. (6) is needed to scale the power spectrum to account for the loss of amplitude when using a nonrectangular window. Since a single FFT has some uncertainty, several FFTs of length L are computed for a given signal and the resulting two-sided power spectrums are averaged together to get a more accurate estimate

$$\bar{S}_{xx}(k) = \frac{1}{M} \sum_{m=1}^M S_{xx}^m(k) \quad (9)$$

where M is the total number of computed two-sided power spectrums, and S_{xx}^m denotes the m th power spectrum. Finally, the continuous PSD is computed from the averaged two-sided power spectrum

$$\tilde{G}_{xx}(k) = 2T_p \bar{S}_{xx}(k) \quad k = 1, \dots, L/2 \quad (10)$$

$$\tilde{G}_{xx}(0) = T_p \bar{S}_{xx}(0) \quad (11)$$

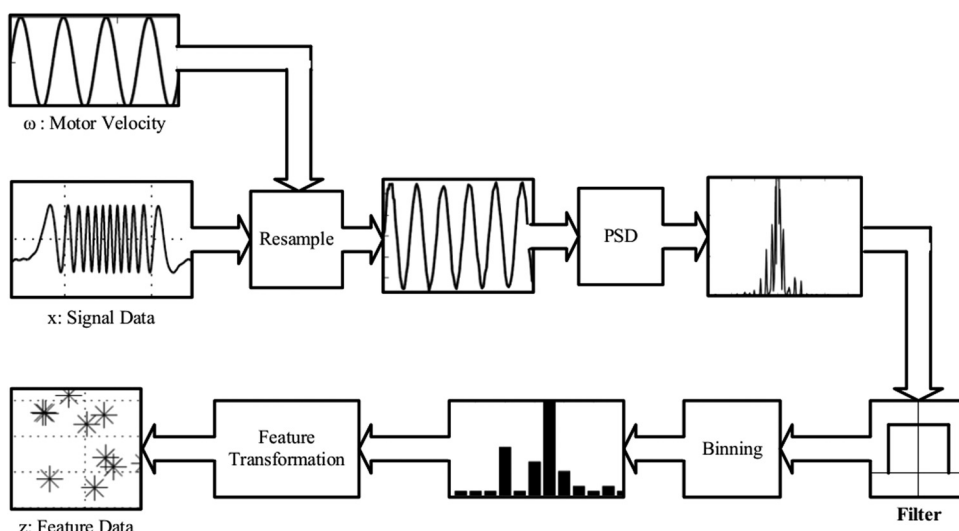


Fig. 3 Proposed feature extraction method

where $T_p = L/F_s$ is the period of the signal sampled with frequency $F_s = 1/T_s$.

2.1.3 Feature Space Transformation. After resampling and PSD computation, the PSD samples are grouped into N -energy bins of size δ_b using a discrete integration method. Since the signal is first translated to the spatial frequency domain, the PSD transforms the data into an order spectrum (as opposed to the frequency spectrum). The resulting binned PSD vector from a single data set consists of N_B elements

$$y = [y_1, y_2, y_3, \dots, y_{N_B}]^T \quad (12)$$

Each of the components of y corresponds to the magnitude of the binned PSD at specific orders for a single trial run. In order to reduce the dimension of the vector, a transformation is needed to map from a space with a large dimension N_B to a smaller dimension D . This may be accomplished using the linear transformation

$$z = Wy \quad (13)$$

The linear transformation (or weight) matrix, $W \in D \times N_B$, maps the binned PSD vector y onto the reduced dimension feature vector z .

A PCA is chosen to obtain the components of the weight matrix using data from a training set. A training set consists of binned PSD computations from signal data collected from a population of known healthy units and units that are known to have defects. The goal of the PCA technique when applied in this manner is to obtain a transformation matrix that weighs the PSD orders that give the most insight into the health of the machine more heavily (i.e., the components that differ between healthy and defective units). The orders that differ in magnitude between the healthy and defective data should produce a larger variance resulting in a larger weighting.

From Eq. (13), the PCA technique maps the vector y onto the feature vector (also known as principal component vector) z by

$$z_i = e_{i1}y_1 + e_{i2}y_2 + e_{i3}y_3 + \dots + e_{iN}y_N \quad (14)$$

The coefficients e_{ij} are the weight matrix coefficients that are equal to the eigenvector components from the PCA. The eigenvectors are ordered from the largest corresponding eigenvalue to the smallest. Therefore, the first principal component z_1 explains the most training set variance, the second component z_2 explains the second most variance, and so on. The components that explain the majority of the variation in the training set are retained while the other components are discarded in order to reduce the number of features.

2.2 Classification. The objective is to assign a class label \hat{w} to an object with true class w . The assignment is based on the measurement or feature vector \vec{z} . The set of possible classes is defined by the set of K classes

$$\Omega = \{w_1, \dots, w_K\} \quad (15)$$

In this application, the object class relates to the health status of an EMA. For instance, the health status may be defined by the set $\Omega = \{\text{"Healthy—Normal Operation,"}, \text{"Unhealthy—Defective Motor Bearing,"}, \text{"Unhealthy—Screw Defect,"}, \dots, \text{"Unhealthy—Unknown"\}}$. This research considers a Bayesian classification approach that utilizes Bayes' theorem to select the class of an object from a set Ω , which are assumed to be mutually exclusive. The class with the minimum amount of risk is the class selected by the Bayesian classifier, which amounts to solving the following equation:

$$\hat{w}_{\text{BAYES}}(z) = \arg \min_{w \in \Omega} \left\{ \sum_{k=1}^K C(w|w_k) p(z|w_k) P(w_k) \right\} \quad (16)$$

The cost function $C(\hat{w}_i|w_k)$ is the penalty of assigning the class \hat{w}_i coming from an object with true class w_k . The prior probability that the object belongs to class w_k before any measurements are taken (unconditional) is $P(w_k)$. Since the classes are assumed to be mutually exclusive, the probability of each class must add up to one

$$\sum_{k=1}^K P(w_k) = 1 \quad (17)$$

The conditional density, $p(z|w_k)$, comes from the distribution of the data from known classes. The model form of the probability density function is assumed known with unknown parameters that are determined from training data. The most common conditional density, and the one used in this work, is normally distributed and may be expressed by the parametric equation

$$p(z|w_k) = \frac{1}{\sqrt{(2\pi)^D |S_k|}} \exp \left(-\frac{1}{2} (z - \mu_k)^T S_k^{-1} (z - \mu_k) \right) \quad (18)$$

The parameters, μ_k and S_k represent the expectation vector (mean) and covariance matrix, respectively, of the random feature vector \vec{z} coming from an object with true class w_k . Assuming that the mean and covariance matrix are unknown, they may be estimated from the training set data by the following equations, respectively:

$$\hat{\mu}_k = \frac{1}{N_k} \sum_{n=1}^{N_k} z_n \quad (19)$$

$$\hat{S}_k = \frac{1}{N_k - 1} \sum_{n=1}^{N_k} (z_n - \hat{\mu}_k)(z_n - \hat{\mu}_k)^T \quad (20)$$

The term N_k represents the number of training samples coming from class w_k .

3 Simulation of Approach

In this section, the feature extraction and fault classification approach is demonstrated with simulated data. The data are generated for what is considered a normal/healthy data set and from two other data sets with distinct fault frequency components. The signals are constructed to be similar to what would be expected from a motor phase current signal for a typical EMA with a 12 pole brushless PMSM.

Consider the following fabricated motor velocity signal (ω_m), which is sinusoidal with a frequency of 5 Hz and a range of 0–40π rad/s (1200 RPM) and the associated motor angle (θ_m)

$$\omega_m(t) = 20\pi(1 + \sin(2\pi 5t)) \quad (21)$$

$$\theta_m(t) = 20\pi t - 2 \cos(2\pi 5t) \quad (22)$$

Let the EMA current be made up of three parts: (1) a fundamental signal, x_f that is characteristic of both a normal/healthy system and one in the presence of a defect, (2) a defect signal, x_d that is periodic with motor position, and (3) a normally distributed noise signal, x_n . The signal is represented by the following equation:

$$x = x_f + x_d + x_n \quad (23)$$

where

$$x_f = 5 \sin(6\theta_m) + 0.1 \sin(2\pi 100t) \quad (24)$$

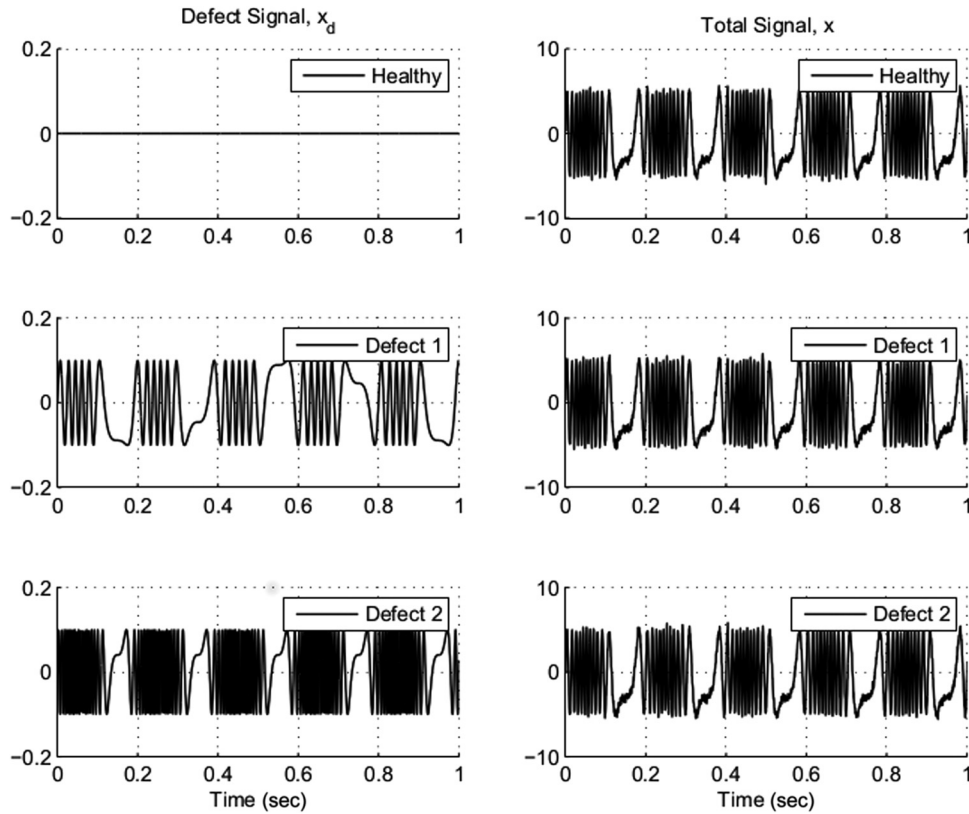


Fig. 4 Generated data: (left)—defect signals, (right)—total signals

$$x_d = \begin{cases} 0 & \text{Healthy} \\ 0.1 \sin(3.125\theta_m) & \text{Defect1} \\ 0.1 \sin(10.5\theta_m) & \text{Defect2} \end{cases} \quad (25)$$

$$x_n \sim N(0, 0.25) \quad (26)$$

The defect and composite signals for the healthy and defective signals are generated with a sampling frequency of 2 kHz and are shown in Fig. 4, over a 1 s interval.

3.1 Feature Extraction. The PSD of the composite signal is computed prior to and after resampling and is shown in Fig. 5. The PSD prior to resampling was computed using a single Hanning window of 4096 points, resulting in a frequency resolution of 0.49 Hz. In this case, the PSD does not appear to be different between the healthy and defective signals. This is due to the fundamental frequency being a multiple of the motor frequency that spreads the frequency content of the signal over the frequency range. Since the fundamental signal dominates, the defective frequency (which is also spread over the frequency range) is not apparent.

The resampled signals are computed with a sampling interval of $\theta_s = 0.002\pi$ radians per sample (1000 samples per revolution). In this case the PSD is computed using a single Hanning window of 2^{14} points, resulting in a frequency resolution of 0.06 orders. The fundamental signal appears at six orders for the healthy and defective signals as expected. In addition, the defective components can also be seen for defect 1 (3.1 orders) and defect 2 (10.5 orders), as desired. Since the signal contains a fundamental component of six orders, an ideal bandpass filter is utilized with a stop band from 5.6 to 6.4 orders. Next, the resampled PSD is grouped into bins of size $\delta_b = 1$ orders over the range of 0–50

orders ($N_b = 50$), and the remaining orders are discarded. The filtered PSD and the binned PSDs are shown in Fig. 6.

The binned data are transformed to a lower-dimensional space through the transformation matrix W . The matrix is obtained by forming a training set matrix consisting of multiple runs of data for each of the three signals and then performing the PCA on the training set matrix. For the simulation, a total of 40 sets of data are generated for each of the three cases—healthy, defect 1, and defect 2. This results in a training set matrix of size $120 \times N_b$. The PCA results in 50 eigenvalues and 50 eigenvectors and the contribution of each eigenvector to the total variance in the training set is shown in Fig. 7. The first two principal components account for about 72% of the total variance, so the remaining 48 principal components are discarded.

The magnitude of the eigenvector components gives an indication of the relative importance of the bins to each principal component. The percentage contribution of each bin to the principal component for the first two principal components is shown in Fig. 8. The largest contributing bin to the first principal component is the 11th bin (31%). This bin has a range from 10 to 11 orders and contains defect 2 (10.5 orders). Bin number 4 is the largest contributor to the second principal component, having a range of 3–4 orders, containing defect 1 (3.125 orders). This result is expected since the values in these bins will be larger when the defect is present, creating a larger variance in the training set.

Note that bins 6, 7, and 8 are also moderate contributors to each principal component. This is likely due to the leakage of the fundamental component into neighboring bins. The contribution of these bins may be reduced by using a different windowing function or increasing the stop band range of the filter. However, the filter stop band range must not be so wide as to cancel out the orders containing the defects.

Since the first two principal components are selected, the transformation matrix (W) is 50×2 . Multiplying the bin values by the transformation matrix for each of the training set runs, reduces the

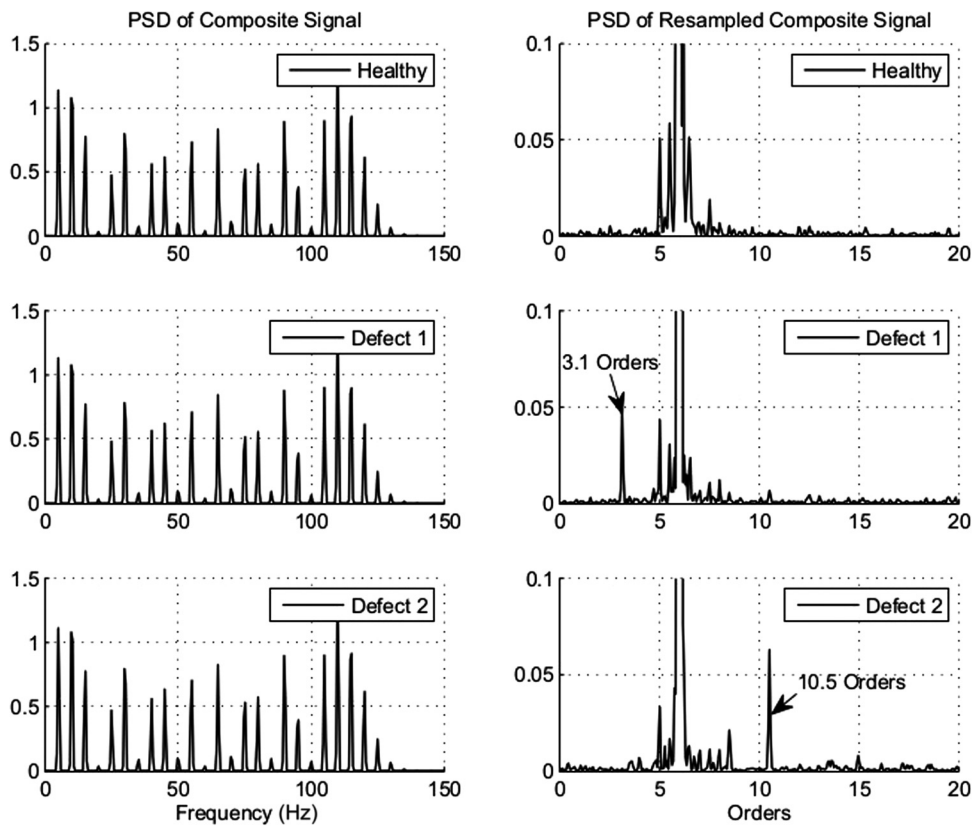


Fig. 5 PSD comparison: (left)—prior to resampling, (right)—after resampling

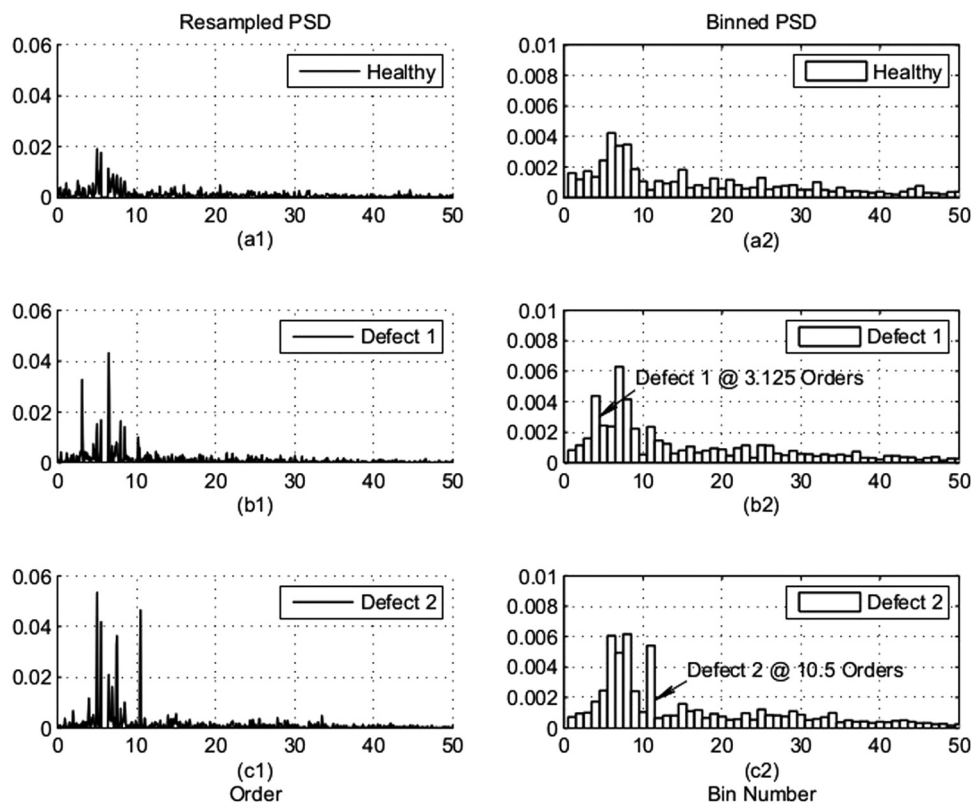


Fig. 6 PSD comparison: (left)—resampled and filtered PSD, (right)—binned PSD

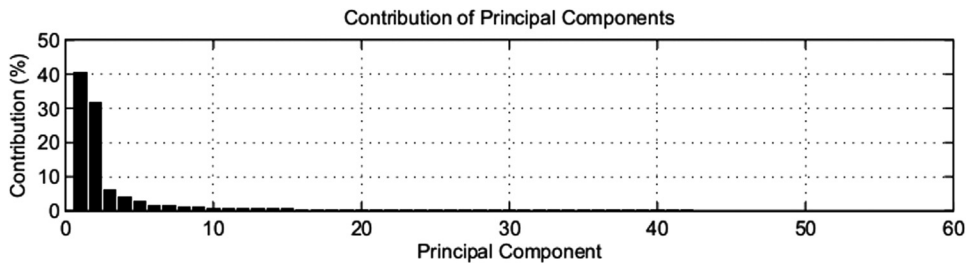


Fig. 7 Principal Component contributions to the total training set variance (72% for first two)

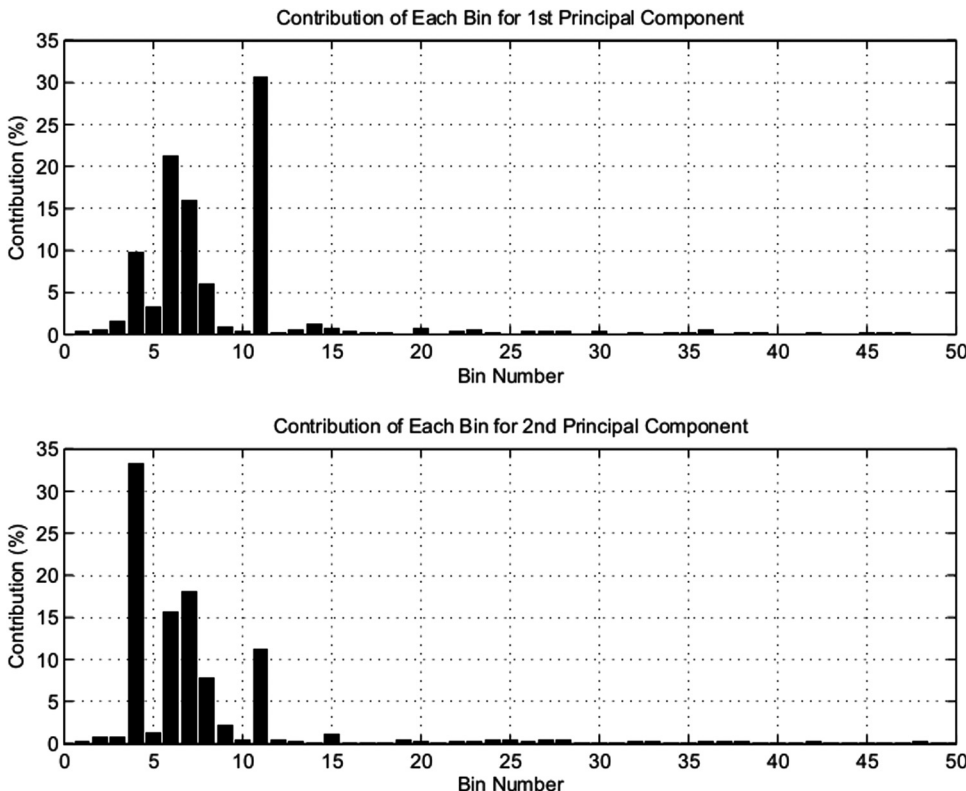


Fig. 8 Contribution of each bin to the first two principal components

feature vector from $N_B = 50$ to $D = 2$ components and results in the scatter plot shown in Fig. 9. The class of each of the data points is indicated in the figure and shows that each class largely occupies a distinct region in the feature space.

3.2 Classification. The feature data obtained are now used to determine whether the data are healthy or contains defect 1 or defect 2. This is done using the Bayesian classification approach presented earlier. In order to perform the algorithm, two probabilities must be determined, $P(w_k)$ and $p(z|w_k)$. For the simulation, there is equal probability of having a signal that is healthy, or contains defect 1 or defect 2. As a consequence, the prior probabilities are set equal

$$P(w_1) = P(w_2) = P(w_3) = 1/3 \quad (27)$$

where the subscripts 1, 2, and 3 denote healthy, defect 1, or defect 2, respectively.

The conditional density, $p(z|w)$ is determined using parametric learning where it is assumed that the distribution is Gaussian with unknown parameters μ_k , and S_k . The parameters are determined from the training set data using Eqs. (19) and (20). Two-

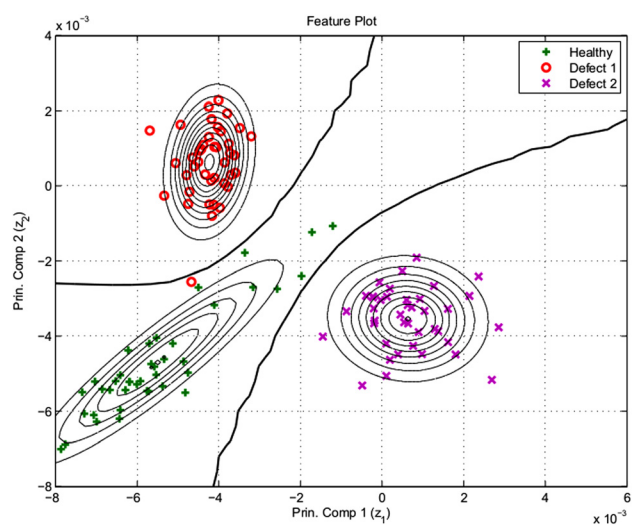


Fig. 9 Feature plot of training set data with class probability densities

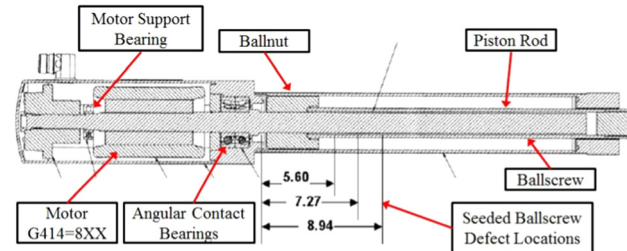


Fig. 10 MOOG MaxForce EMA (G414-8xx): Technical specifications and cross section

dimensional contour plots of the conditional probability densities for the training set data are shown in Fig. 9 along with the feature data. Note that a normal distribution is not a requirement of the proposed approach. It is used in this work as a commonly assumed distribution in practice and is also used later for the experimental results. Future work is planned in a more rigorous distribution determination approach.

The Bayesian classifier predicts the class of an object by assigning the class with the minimum risk according to Eq. (16). Using a uniform cost function results in the decision boundaries shown in Fig. 9, which accurately classifies the three health class types for the training set data. The result shows 100% of the healthy and defect 2 samples are correctly isolated, and 39/40 or 97.5% of the defect 1 samples are correctly classified. The one misclassified defect 1 sample is classified as healthy (false negative).

4 Experimental Results

The proposed approach is now applied using data from three Moog Industrial MaxForce EMAs operating in a laboratory environment on two different test rigs. The table on top of Fig. 10 shows the technical specification of the G414-8xx MaxForce EMA. First, a ball bearing defect is seeded in one EMA at the motor end and is installed on an active load cell operating at MOOG. A second EMA with three seeded ball screw defects (BSD) is operated in a passive load test rig at RIT. A no defect EMA is also utilized at both test location to provide healthy training data for classification.

The MaxForce EMA itself includes a three phase PMSM that responds to voltage commands to provide rotational output of a screw rigidly coupled to the rotor. A nut is coupled to the screw by steel balls that circulate along the single race of the screw. Rotational motion of the screw is converted to translational

Table 1 Feature extraction parameters

Parameter	Description	Value
θ_s	Spatial sampling period	0.02π rad/sample
δ_b	Bin size	1 order
$C(w w_k)$	Cost function	Uniform
$P(w_k)$	Prior probability	0.5 (equal)

motion by constraining the ball-nut so that it may only traverse along the screw. This translation of the nut provides the output motion of the piston rod. (Note that according to Eq. (3), the fundamental current frequency for this motor is, $f_e/f_r = 6$.)

A simplified cross-sectional view of the EMA and its specifications are shown in Fig. 10 along with the locations of the seeded defects. This figure also shows all of the instrumentation used on both test apparatus. Sections 4.1 and 4.2 describe the specific nature of the result of each experiment.

The EMA is controlled using a nested two feedback architecture. The outer loop is position control of the rod end of the EMA with a LVDT providing a feedback measurement to a dSpace real-time controller (DS1103) running an embedded control algorithm. This controller outputs an EMA motor velocity command to a MOOG T200-510 servo drive. The EMA and T200 perform the inner loop speed control that uses an internal resolver and motor phase current feedback signals to produce compensated voltage commands to the motor coil windings. The experimental tests used in this work are a desired position profile command (sine, triangle, etc.) to the dSpace controller with the T200 subsequently controlling motor velocity to achieve the desired position. Figure 11 shows this signal flow.

The dSpace computer also commands the active load actuator controller and provides the data acquisition and signal scaling. Position feedback is provided by an externally mounted LVDT and an accelerometer is mounted to the EMA housing near the motor angular contact bearing. The T200 has two configurable analog outputs for internal measurements, and for this work are set to EMA motor angular velocity and angular position. In addition, current measurements for all three phases (UVW) of the T200 command to the EMA are recorded.

For the feature extraction and classification portion of the experimental results, both the ball bearing and ball screw defects experiments use the information provided in Table 1. The spacial sampling period is used to convert from the time to position domain with the angular sampling period chosen so that the PSD would contain a maximum of 100 orders. The sampling period is

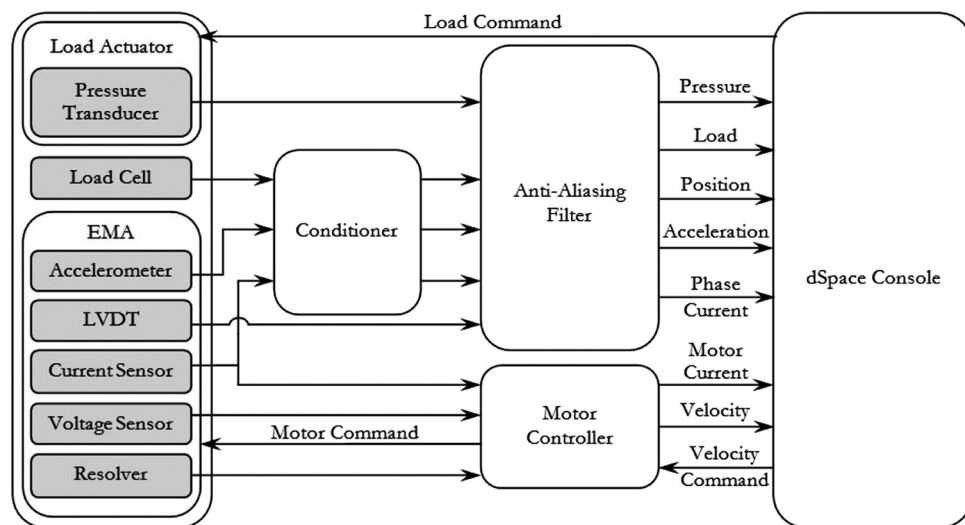


Fig. 11 EMA laboratory signal diagram

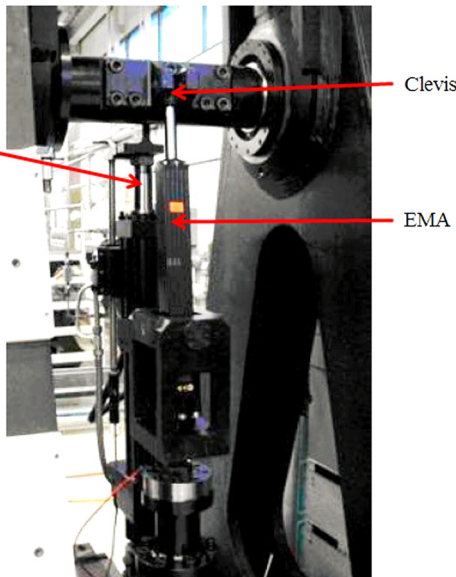


Fig. 12 Ball Bearing Defect (BBD)—EMA test fixture at MOOG

also small enough to prevent signal aliasing. For the Bayesian classification, a uniform cost function and equal prior probability of classes is assumed.

Not every step of the proposed method is illustrated in the following figures for each defect and condition tested. Rather a selection of plots is shown illustrating the method, across the various tests, culminating in a validation data set classification for all test scenarios.

4.1 BBD. The first EMA is considered normal/healthy and the other (which will be referred to as the degraded EMA) has an angular contact bearing with an inner ring defect and 75% of the normal grease applied to it. The corresponding mechanical defect frequency for the inner ring defect is $f_{IR}/f_r = 6.123$.

4.1.1 Test Setup. The EMA is suspended vertically in the test fixture with the piston rod end attached to a rotating clevis near the top of the fixture. On the opposite end of the clevis, the hydraulic actuator is also attached and suspended vertically. The hydraulic load actuator contains an electrohydraulic servovalve that is commanded in a closed loop fashion to control the load applied to the EMA. This is accomplished by a differential pressure transducer on the hydraulic load actuator that senses the pressure at the actuator piston. A load cell is included in the test fixture to measure the actuator load. The test fixture with EMA installed is shown in Fig. 12.

The sampling rate of the controller is 48 kHz with the data acquisition measurements collected at 12 kHz for this test setup. Signal conditioning filters are set at 15 kHz and used prior to analog to digital conversion to prevent signal aliasing.

4.1.2 Results. In order to demonstrate the performance of the health monitoring approach, data from the healthy and degraded EMAs are collected over the operating conditions shown

in Table 2, which are typical of conditions for an Aircraft Spoiler EMA duty cycle. Data are collected from each condition 20 times for both the healthy and degraded EMAs, with motor phase U current and radial accelerometer measurements used as the health monitoring signals. The first ten data sets for each condition are used for training to obtain the transformation matrix and estimating the parameters of the probability densities for the Bayesian classification. The remaining ten data sets are used for validation and testing. Training is done on a per condition basis, i.e., training is done separately for each condition so that Bayesian decision boundaries are tailored to the operating condition. For each test condition, the parameter settings shown in Table 1 are used for both current and vibration signals.

The results for condition 1 for the healthy EMA are shown in Fig. 13. First, the EMA position command and LVDT position feedback are shown followed by the motor speed command to the MOOG T200 controller with the resolver feedback measurement. The corresponding accelerometer signal placed at the main motor bearing is shown. The signal is resampled and a PSD is determined.

To illustrate the strength of the proposed approach, a comparison is performed with the phase current measurement using the widely used FFT technique for the degraded EMA. Figure 14 shows the raw (preresampled) phase A current signal along with the corresponding Hanning windowed FFT. It is clear from this plot little abnormal frequency content stands out with a continuous band from 0 to 250 Hz, which corresponds directly to the time-varying frequencies associated with the current measurement. The peak magnitude occurs at approximately 250 Hz and corresponds to the predominate time spent at 2500 rpm motor speed as expected. ($\text{Freq (Hz)} = \text{motor pole pairs (6)} \times (\text{motor velocity (rpm)} \times (1/60))$) The resample PSD of phase current is described next and depicts clear frequency content of interest.

For a comparison of the phase current and accelerometer measurements, the final result after the binning process for condition 1 is shown for both in Fig. 15. The binned PSD plot clearly shows the presence of the defect in the accelerometer data, with peaks spaced about six orders apart corresponding to the frequency of an inner ring defect. The current signal also shows larger sidebands around the fundamental component possibly due to the less amount of bearing grease. The fundamental frequency harmonics line up exactly with the defect harmonics so the inner ring defect is not clear in the current PSD signal.

Using PCA to obtain the transformation matrix, the number of features is reduced to two and accounts for 80% of the training set variance. A scatter plot of the resulting feature vector for the ten healthy and ten defective test set samples is shown in Fig. 16 from the current and accelerometer data. Note the wide degree of separation between the healthy and degraded EMA samples from the accelerometer signal data. The Bayes decision boundaries based on a normal distribution of the data are also shown and result in a 100% correct classification percentage, with no false positives or false negatives. A normal distribution for the conditional density function is assumed but it is important to note that this is not a requirement and if more data points are available a more precise selection should be performed.

A 100% correct classification also results for the current signal, but the separation between healthy and defective EMA samples is less distinctive. However, it is noteworthy that phase current is an inexpensive and reliable measurement to collect that could

Table 2 BBD—MOOG MaxForce EMA test profile

Condition no.	Command type	Actuator command			Load command		Data set uses	
		Bias (in)	Amp. (in)	Freq. Hz	Spring rate (lbf/in)	Bias (lbf)	Training	Test
1	Sine	0.10	1.90	0.70	0	116	1–10	11–20
2	Triangle	-0.90	1.40	1.00	0	278	1–10	11–20

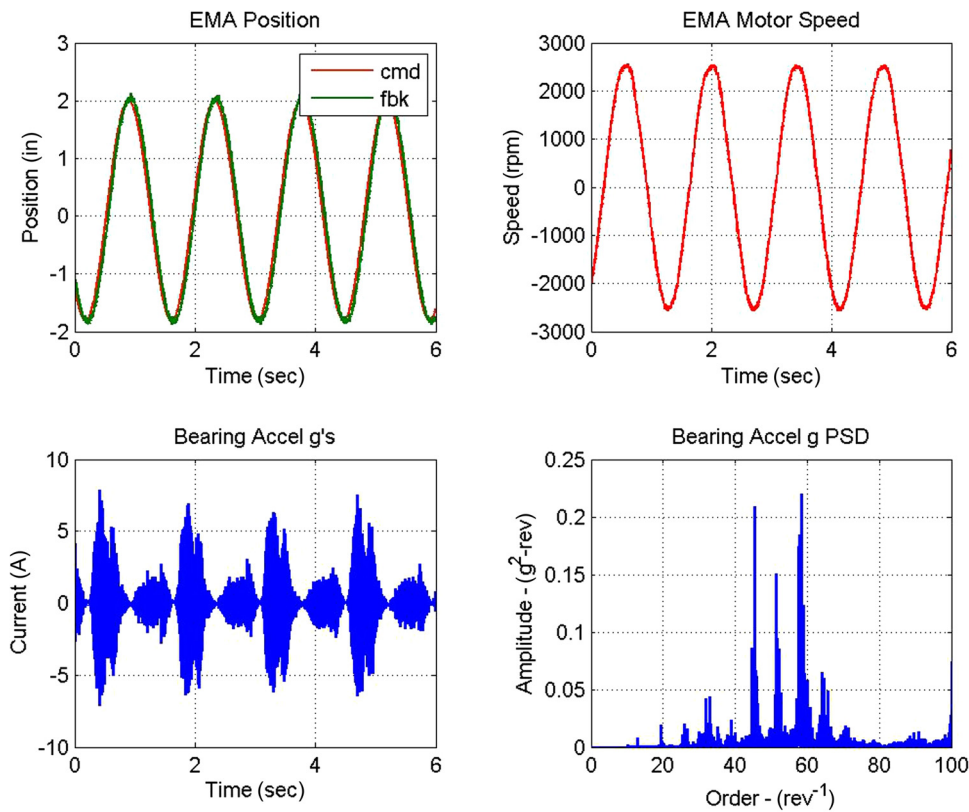


Fig. 13 BBD—condition 1 (degraded): EMA position—(upper left), motor speed—(upper right), accelerometer—(lower left), PSD—(lower right)

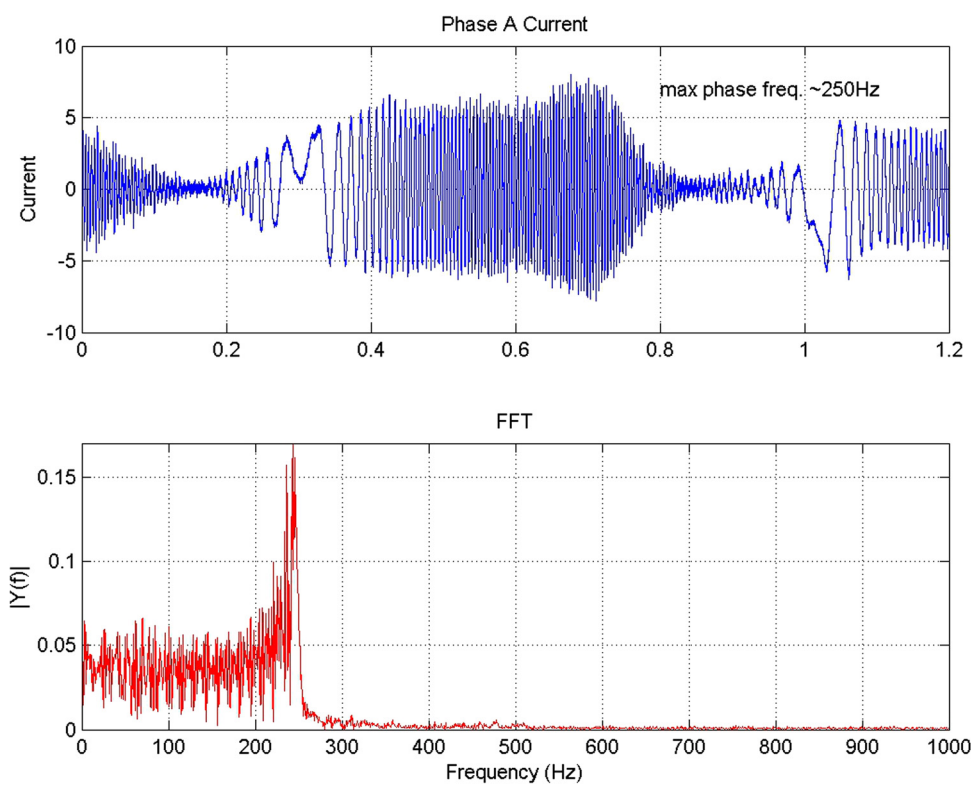


Fig. 14 BBD—condition 1 (degraded): phase A current—(top), FFT of raw phase current (freq. resolution = 0.73)—(bottom)

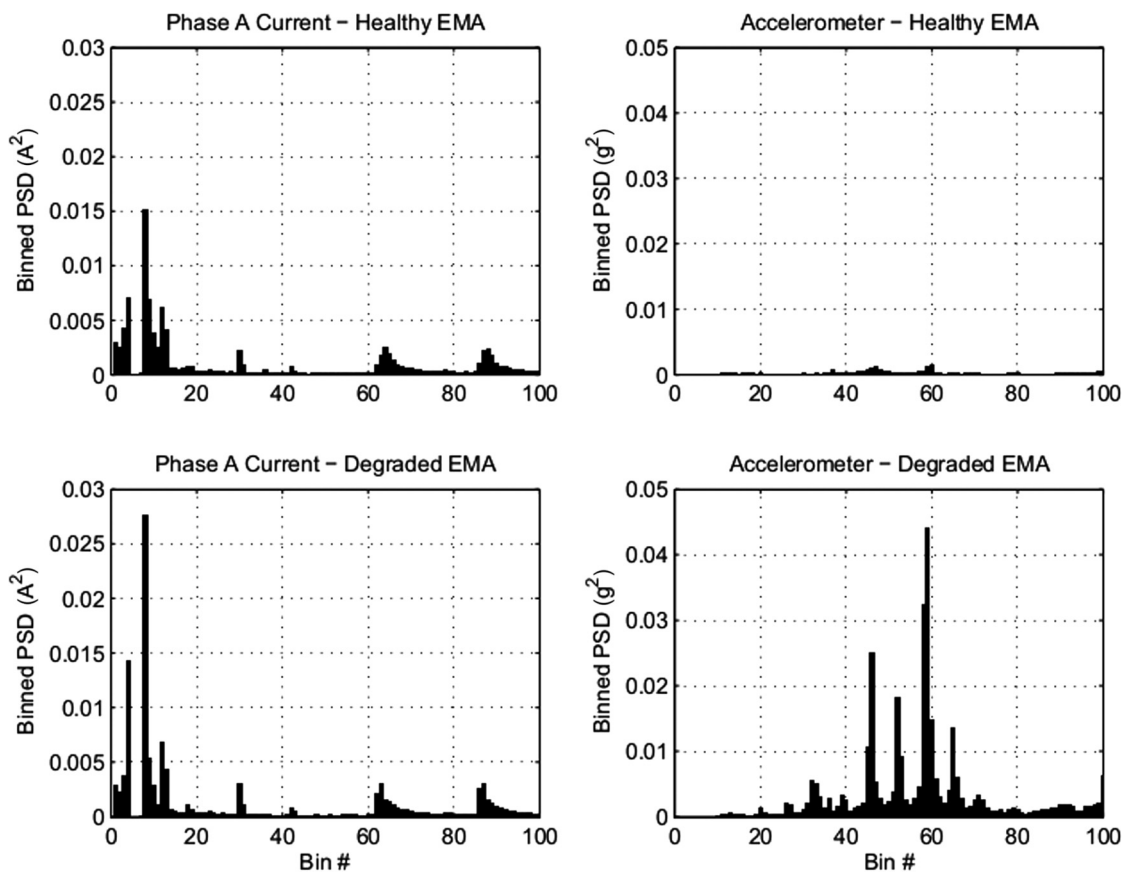


Fig. 15 BBD—condition 1: binned PSD

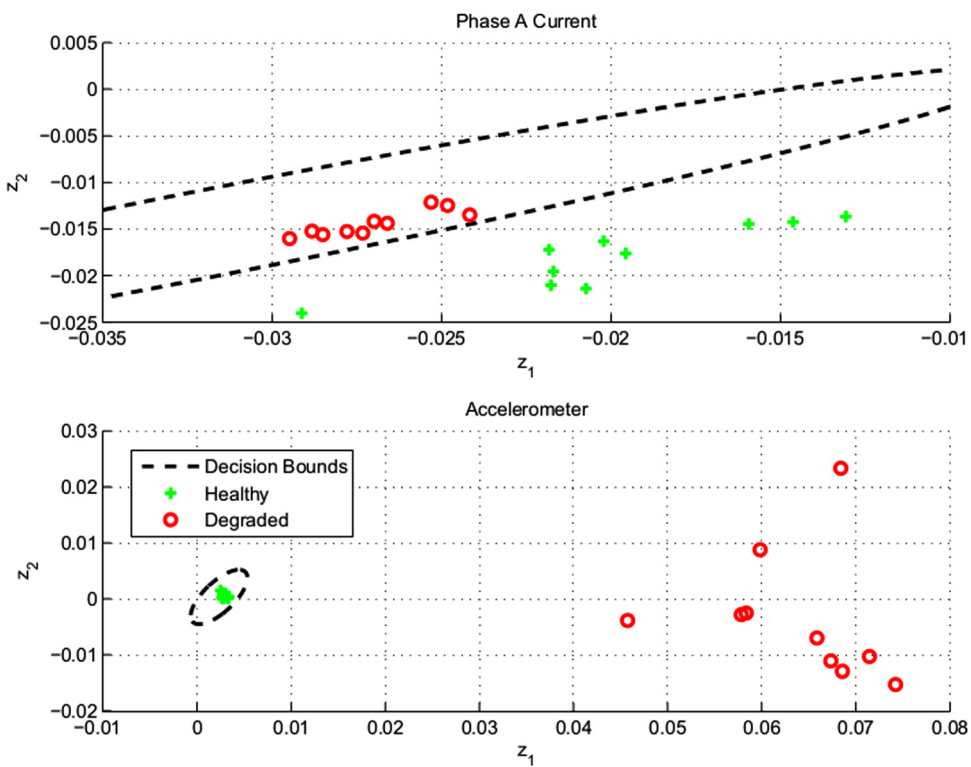


Fig. 16 BBD—condition 1 (validation data): feature plot with Bayesian classification bounds (0%, 0% miss classification, respectively)

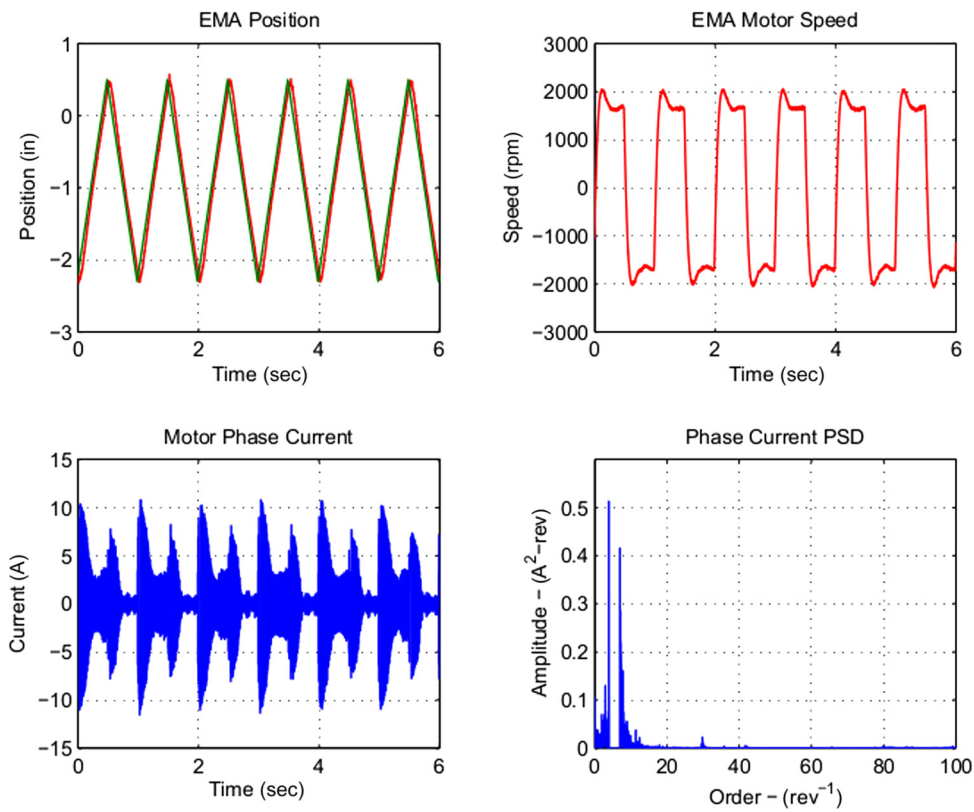


Fig. 17 BBD—condition 2 (degraded): EMA position—(upper left), motor speed—(upper right), phase current—(lower left), PSD—(lower right)

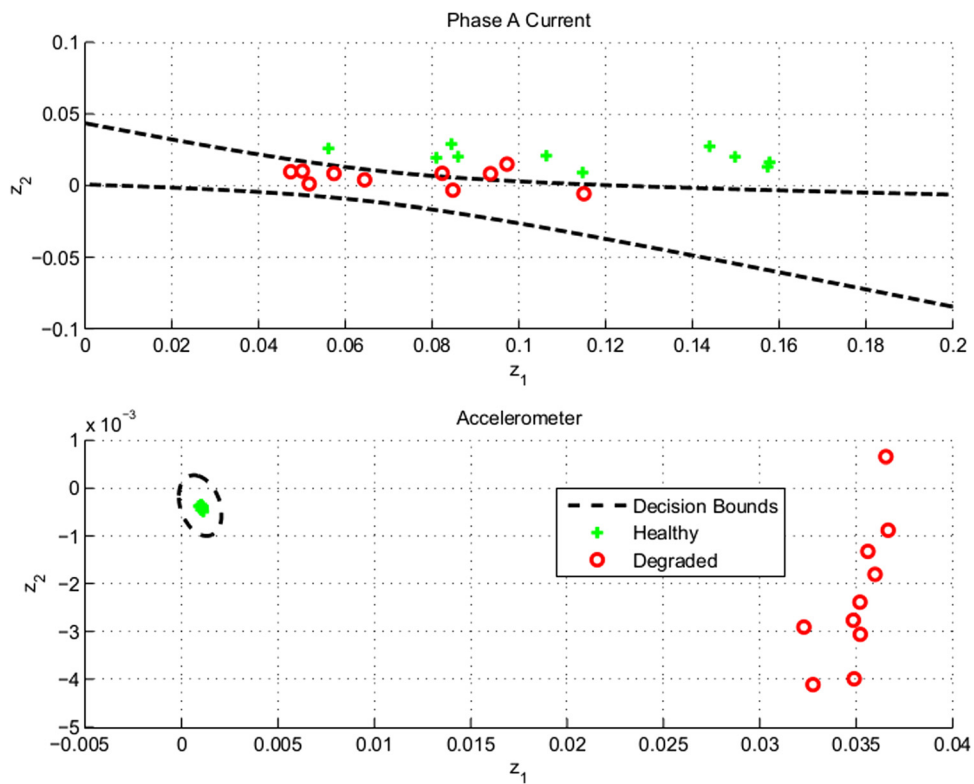


Fig. 18 BBD—condition 2 (validation data): feature plot With Bayesian classification bounds (0%, 15% miss classification, respectively)

Table 3 BSD—MOOG MaxForce EMA test profile

Condition no.	Command type	Actuator command			Load command		Data set uses	
		Bias (in)	Amp. (in)	Freq. Hz	Spring rate (lbf/in)	Bias (lbf)	Training	Test
1	Sine (H)	1.0	0.85	0.67	1275	0	1–20	41–60
	Sine (D)	1.0	0.85	0.67	1275	0	21–40	61–80
2	Triangle (H)	0.9	0.90	1.00	1275	0	1–20	41–60
	Triangle (D)	0.9	0.90	1.00	1275	0	21–40	61–80

easily be inherent to the EMA motor controller, unlike a costly and delicate dedicated accelerometer mounted to the EMA body.

Similar results are also obtained for condition 2 with the resulting phase current signal plot and corresponding binned PSD shown in Fig. 17. The feature plot and Bayesian classification results for the test set data are shown in Fig. 18. In this case, the current signal had 85% correct classifications with three false negatives and zero false positives.

4.2 BSD. The approach is now applied to a different failure mode, ball screw defects, again using data from two Moog MaxForce EMAs in a laboratory environment. Again, the first EMA is considered normal/healthy and the other (degraded) EMA has a seeded BSD at three distinct locations (see Fig. 10). The BSD experiments are conducted at RIT in a similar test cell with identical instrumentation as those conducted at MOOG.

4.2.1 Test Setup. The laboratory setup consists of the EMA, a passive spring-based load, position, acceleration, and current sensing devices, a test fixture, a Moog T200 motor controller, power and signal conditioning equipment, and a PC-based computer interfacing a dSpace rapid prototyping embedded platform. The EMA is installed in a heavily modified version of a 787

spoiler test rig. Since the EMA tested in this work is a physically larger EMA the test fixture needed to be augmented by retrofitting the trunnion mounting attachment as well as a total replacement and redesign of the rod end connection. The primary loading for the EMA is through two 637.5 lb/in compression springs. These springs provide an accurate and linear load to the EMA that can easily be calculated through calibration and displacement measurement. The test fixture with EMA installed is shown in Fig. 1. The instrumentation in Fig. 10 and the signal flow diagram in Fig. 11 are accurate for this test setup save for the load actuator since this test setup is not actively load controlled. A load measurement is taken indirectly from the LVDT position measurement and assuming a linear spring constant. The sampling rate of the controller and the DAQ is set to 10 kHz and there is no anti-aliasing filter required.

4.2.2 Results. Similar to the ball bearing defect case data from the healthy and degraded EMA are collected with the operating conditions shown in Table 3. Eighty data sets are collected for each condition, 40 sets each from the healthy and degraded EMA, with motor phase current and radial accelerometer measurements used as the health monitoring signals. The first 40 data sets for each condition are used for training to obtain the transformation matrix (W) and estimating the parameters of the probability

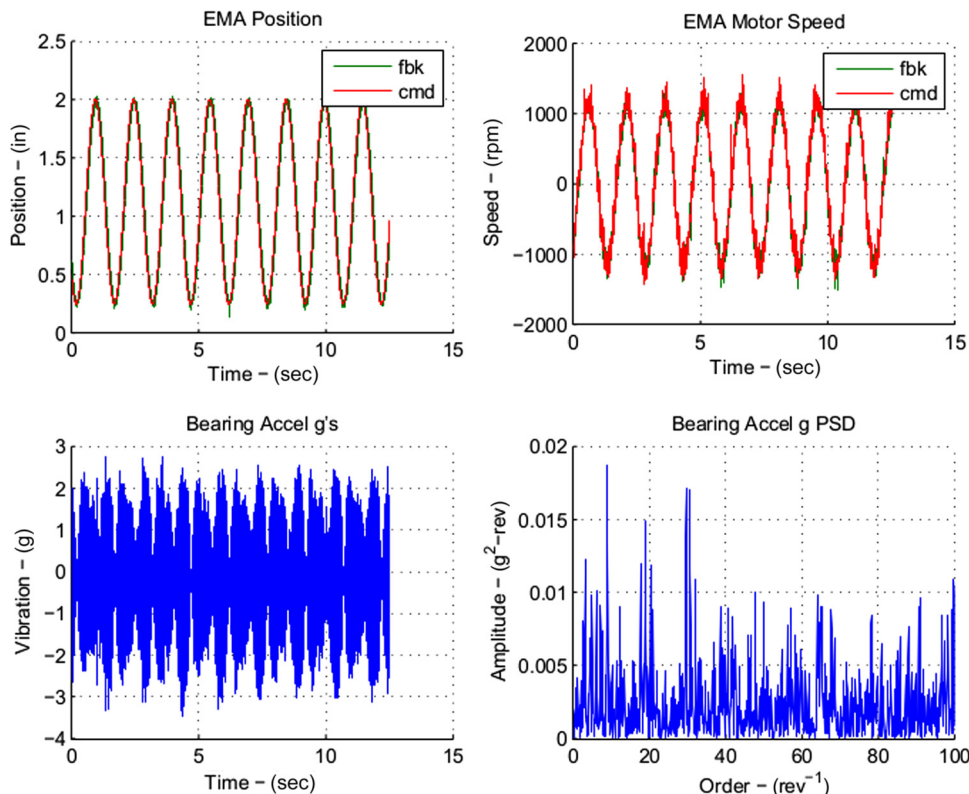


Fig. 19 BSD—condition 1 (healthy): EMA position—(upper left), motor speed—(upper right), accelerometer—(lower left), PSD—(lower right)

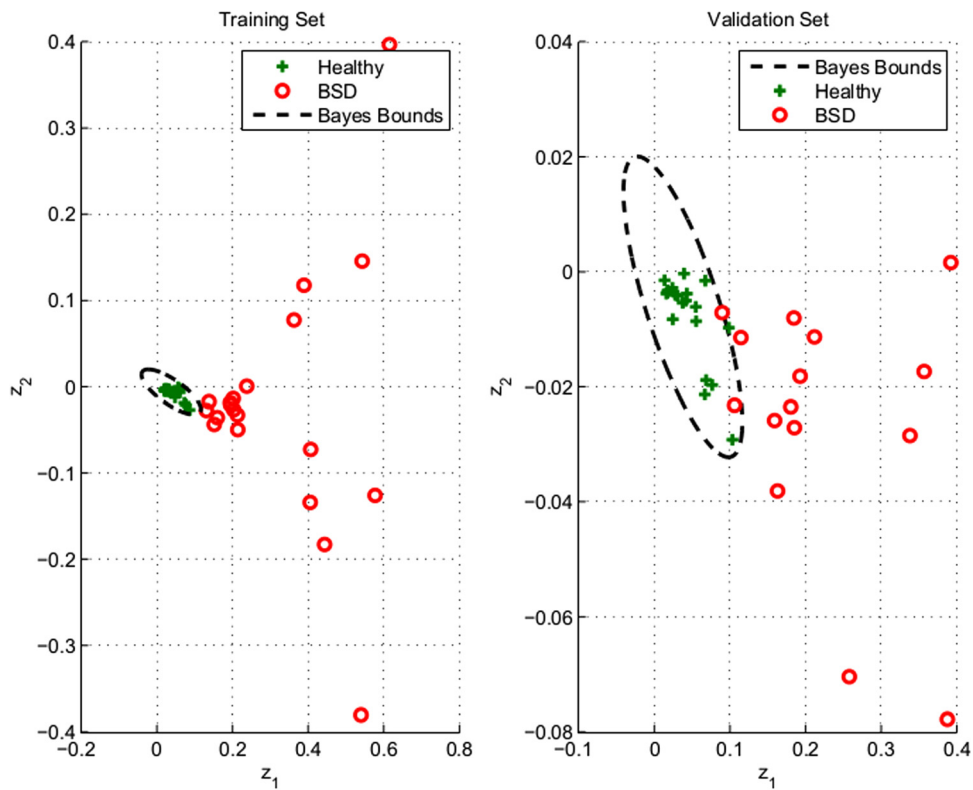


Fig. 20 BSD—condition 1: classification—training data—(left), validation data—(right) (0%, 5% misclassification, respectively)

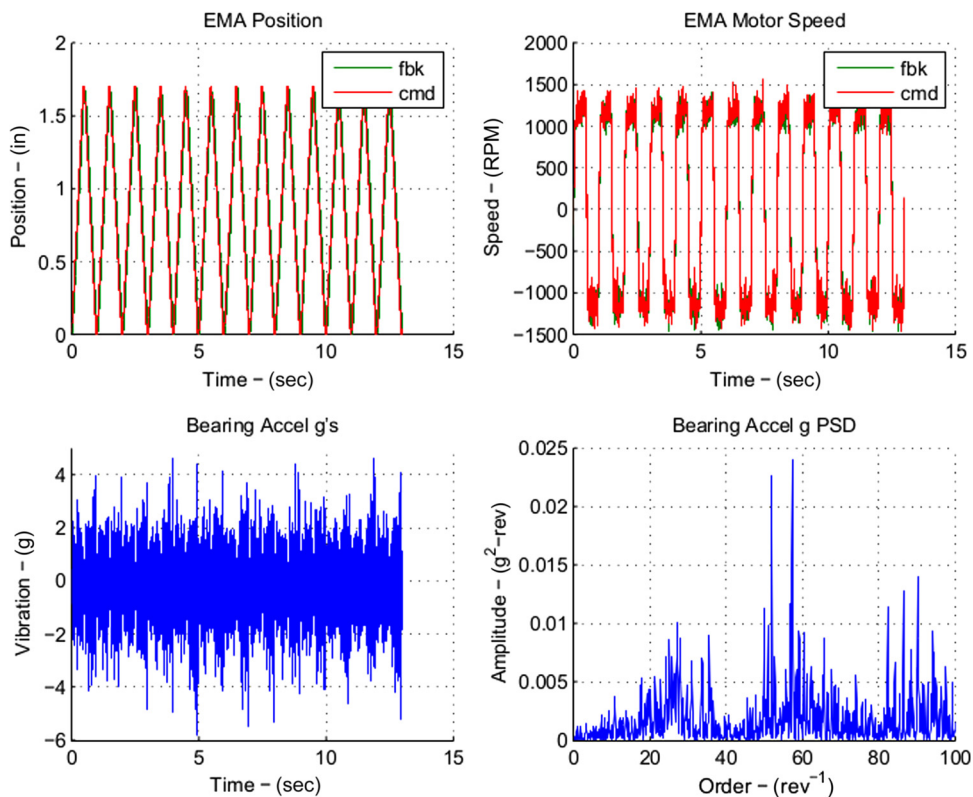


Fig. 21 BSD—condition 2: EMA position—(upper left), motor speed—(upper right), accelerometer—(lower left), PSD—(lower right)

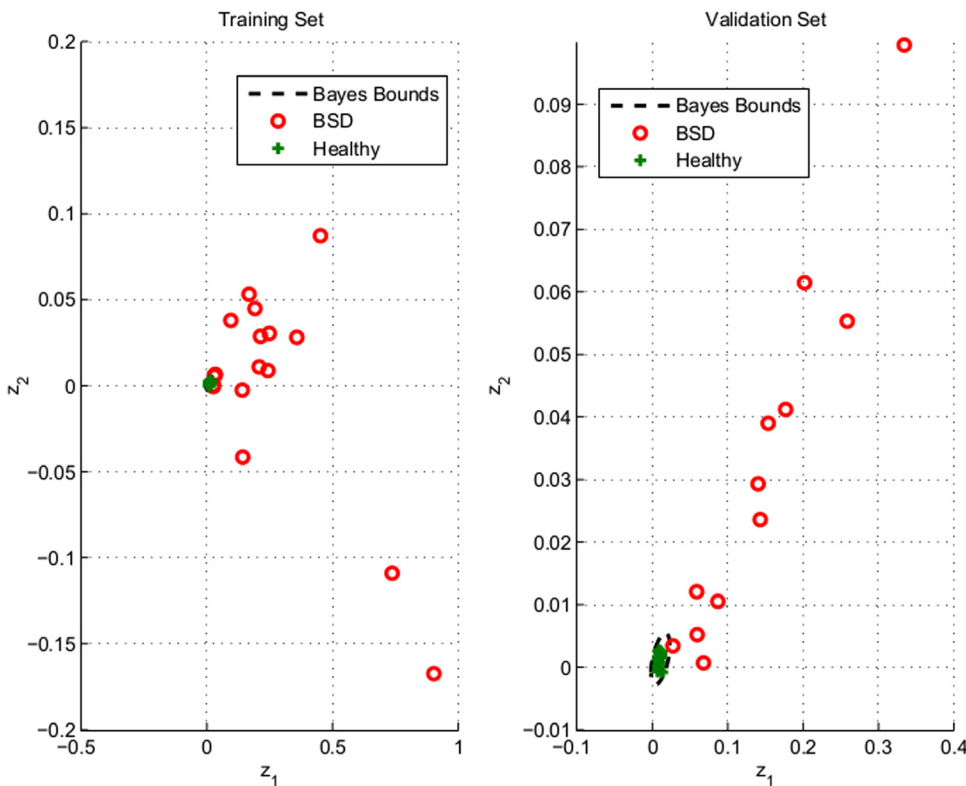


Fig. 22 BSD—condition 2: classification—training data—(left), validation data—(right) (0%, 2.5% miss classification, respectively)

densities ($\hat{\mu}_k, \hat{S}_k$) for the Bayesian classification. The remaining 40 data sets are used for validation. Training, again, is done on a per condition basis. For each test, the parameter settings following the BBD case are applied. (Table 1)

The results for condition 1 for the healthy EMA are shown in Fig. 19. Again the position and motor velocity is shown with feedback measurement along with the raw accelerometer signal and corresponding PSD from the resampled signal. The PSD is binned and followed by a PCA analysis. Two principle components are used in this work thereby reducing the feature vector to two. Again, this is chosen because of the relatively high degree of representation by these two components, but also for ease of visual representation of the technique.

The proposed method is applied to each measurement signal (independently) for all training data sets used in both conditions. A scatter plot of the resulting feature vector using the accelerometer signal for 20 healthy and 20 defective ball screw test set samples is shown in Fig. 20 along with Bayesian decision boundaries determined following analysis of the training data. The figure also shows the classification result when applied to the validation data sets as well. Clearly both meet with a very high degree of accuracy with few missed classifications (0% training, 5% validation).

Similar results were also obtained for condition 2 (triangular wave command) with the resulting EMA position, motor speed, vibration, and PSD shown in Fig. 21. The feature plot and Bayesian classification results for the test and validation data sets are shown in Fig. 22. Again the accelerometer based approach had a near flawless performance with a 100% correct classification rate for the training set and just one misdiagnosis for the validation set.

The motor phase current measurement signal did not show as strong of a classification when used for this type of BSD as it did with the bearing defect. This is likely due to the nonstationary nature of the defect that could not be accommodated by the resampling technique.

5 Conclusion and Future Work

This paper presented a data-driven approach to EMA condition monitoring based on frequency domain feature extraction. Simulation and laboratory results showed that the technique is capable of classifying the condition of an EMA over nonsteady speeds and loads. Accelerometer data are especially successful in exposing and isolating both bearing and ball screw fault signatures. Motor current data are also successful for bearing failure, but better results may have been obtained if the seeded inner ring defect fault signature had not overlapped with the fundamental current signature due to the electrical frequency of the motor. This technique is especially suited for isolating previously characterized faults, but health monitoring may be improved by the addition of a novelty detector to allow anomalous behavior from normal to be detected, even if it is not previously characterized. Further details are found in the following works [19–21].

Future work will also include collecting data from EMAs with other common EMA faults to further assess the ability of the technique for isolating multiple faults. Due to resource constraints experimental testing utilized the same units for testing and validation. Ideally, multiple units would be used for training and separate units would be used for validation. In addition, a classifier that is trained on data from multiple test conditions will also be evaluated so that only one trained classifier is needed. From a theoretical perspective, future work is planned on conditional density function selection based on the distribution of the PCA results.

References

- [1] Rosero, J., Ortega, J., Aldabas, E., and Romeral, L., 2007, "Moving Towards a More Electric Aircraft," *IEEE Aerosp. Electron. Syst. Mag.*, **22**, pp. 3–9.
- [2] Bottem, L. S., Whitley, R. C., and King, D. A., 2000, "Flight Control Actuation Technology for Next Generation All-Electric Aircraft," *Technol. Rev. J.*, pp. 55–68.

- [3] Hao, L., Jinsong, Y., Ping, Z., and Xingshan, L., 2009, "A Review on Fault Prognostics in Integrated Health Management," The Ninth International Conference on Electronic Measurement and Instruments.
- [4] Smith, M., Byington, C., Watson, M., Bharadwaj, S., Swerdon, G., Goebel, K., and Balaban, E., 2009, "Experimental and Analytical Development of Health Management for Electro-Mechanical Actuators," IEEE Aerospace Conference, pp. 1–14.
- [5] Byington, S. C., Watson, M., Edwards, D., and Stoelting, P., 2004, "A Model-Based Approach to Prognostics and Health Management for Flight Control Actuators," IEEE Aerospace Conference Proceedings, Vol. 6, pp. 3551–3562.
- [6] Balaban, E., Bansal, P., Stoelting, P., Saxena, A., Goebel, K., and Curran, S., 2009, "A Diagnostic Approach for Electro-Mechanical Actuators in Aerospace Systems," IEEE Aerospace Conference, pp. 1–13.
- [7] Bodden, D., Scott Clements, N., Schley, B., and Jenney, G., 2007, "Seeded Failure Testing and Analysis of an Electro-Mechanical Actuator," IEEE Aerospace Conference, pp. 1–8.
- [8] Baybutt, M., Nanduri, S., Kalgren, P., Bodden, D., Clements, N., and Alipour, S., 2008, "Seeded Fault Testing and In-Situ Analysis of Critical Electronic Components in EMA Power Circuitry," IEEE Aerospace Conference, pp. 1–12.
- [9] Byington, C., Watson, M., and Edwards, D., 2004, "Data-Driven Neural Network Methodology to Remaining Life Predictions for Aircraft Actuator Components," IEEE Aerospace Conference Proceedings, Vol. 6, pp. 3581–3589.
- [10] Brown, D., Georgoulas, G., Bae, H., Vachtsevanos, G., Chen, R., Ho, Y., Tannenbaum, G., and Schroeder, J., 2009, "Particle Filter Based Anomaly Detection for Aircraft Actuator Systems," IEEE Aerospace Conference.
- [11] Romeral, L., Rosero, J., Espinosa, A., Cusido, J., and Ortega, J., 2010, "Electrical Monitoring for Fault Detection in an EMA," *IEEE Aerosp. Electron. Syst. Mag.*, **25**, pp. 4–9.
- [12] Huh, K.-K., Lorenz, R., and Nagel, N., 2009, "Gear Fault Diagnostics Integrated in the Motion Servo Drive for Electromechanical Actuators," IEEE Energy Conversion Congress and Exposition, pp. 2255–2262.
- [13] Zhou, W., Habetler, T., and Harley, R., 2007, "Stator Current-Based Bearing Fault Detection Techniques: A General Review," IEEE International Symposium on Diagnostics for Electric Machines, Power Electronics and Drives, pp. 7–10.
- [14] Malhi, A., and Gao, R., 2004, "PCA-Based Feature Selection Scheme for Machine Defect Classification," *IEEE Trans. Instrum. Meas.*, **53**, pp. 1517–1525.
- [15] Zhang, B., Georgoulas, G., Orchard, M., Saxena, A., Brown, D., Vachtsevanos, G., and Liang, S., 2008, "Rolling Element Bearing Feature Extraction and Anomaly Detection Based on Vibration Monitoring," 16th Mediterranean Conference on Control and Automation, pp. 1792–1797.
- [16] Rajagopalan, S., Habetler, T., Harley, R., Sebastian, T., and Lequesne, B., 2005, "Current/Voltage Based Detection of Faults in Gears Coupled to Electric Motors," IEEE International Conference on Electric Machines and Drives, pp. 1780–1787.
- [17] Knight, A., and Bertani, S., 2005, "Mechanical Fault Detection in a Medium-Sized Induction Motor Using Stator Current Monitoring," *IEEE Trans. Energy Convers.*, **20**, pp. 753–760.
- [18] Eren, L., and Devaney, M., 2003, "Motor Current Analysis via Wavelet Transform With Spectral Post-Processing for Bearing Fault Detection," Proceedings of the 20th IEEE Instrumentation and Measurement Technology Conference, Vol. 1, pp. 411–414.
- [19] Chirico, A., Kolodziej, J., and Hall, L., 2012, "A Data Driven Frequency Based Feature Extraction and Classification Method for EMA Fault Detection and Isolation," Proceedings of the 2012 ASME Dynamic Systems and Control Conference, Fort Lauderdale, FL, Oct. 17–19, ASME Paper No. DS-2012-MOVIC2012-8749, pp. 751–760.
- [20] Chirico, A., and Kolodziej, J., 2012, "Fault Detection and Isolation for Electro-Mechanical Actuators Using a Data-Driven Bayesian Classification," *SAE Int. J. Aerosp.*, **5**(2), pp. 494–502.
- [21] Chirico, A., 2012, "A Data Driven Frequency Based Method for Electrical-Mechanical Actuator Condition Monitoring," M.S. thesis, Rochester Institute of Technology, Rochester, NY.